

Freeform Liquid 3D Printing of Soft Functional Components for Soft Robotics

Théo Calais, Naresh D. Sanandiya, Snehal Jain, Elgar V. Kanhere, Siddharth Kumar, Raye Chen-Hua Yeow, and Pablo Valdivia y Alvarado*



Cite This: *ACS Appl. Mater. Interfaces* 2022, 14, 2301–2315



Read Online

ACCESS |



Metrics & More



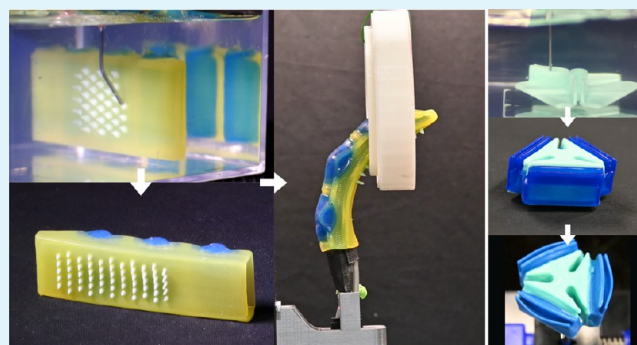
Article Recommendations



Supporting Information

ABSTRACT: Freeform liquid three-dimensional printing (FL-3DP) is a promising new additive manufacturing process that uses a yield stress gel as a temporary support, enabling the processing of a broader class of inks into complex geometries, including those with low viscosities or long solidification kinetics that were previously not processable. However, the full exploitation of these advantages for the fabrication of complex multilayered structures has been hindered by difficulties in controlling the interfaces between inks and supports. In this work, an in-depth study of the rheological properties and interfacial stabilities between a nanoclay-modified support and silicone-based inks enabled a better understanding of the impact printing parameters have on the extruded filament morphology, and thus on printing resolutions. With these improvements, the fabrication of functional multimaterial pneumatic components applied to soft robotics could be demonstrated, exhibiting superior capabilities compared to casting or traditional extrusion-based additive manufacturing in terms of geometric freedom (overhanging and multimaterial structures), tunability of the component's functionality, and robustness between different phases. Overall, the full exploitation of FL-3DP advantages enables a broader design space for features and functionalities in soft robotic components that require complex and robust combinations of materials.

KEYWORDS: soft robotics, additive manufacturing, support bath, freeform fabrication, gripper, embedded sensors



1. INTRODUCTION

Freeform liquid three-dimensional printing (FL-3DP) has emerged as a promising enhancement of extrusion-based additive manufacturing technologies.^{1,2} This technique relies on the use of a suspension medium as a temporary support, enabling the extrusion of a wider range of inks, including those with low viscosities or long solidification kinetics. While progress in this field has been mainly driven by fabrication needs in biomedical applications and tissue engineering (using delicate bioinks and hydrogels),^{1,2} the applicability to other fields remains to be demonstrated. Among them, soft robotics is of particular interest as enabling multimaterial combinations and advanced functionalities in highly complex geometries are crucial for enhancing the performance of soft robots.^{3–5} The fabrication of multimaterial soft robots still mainly relies on casting/molding processes^{6,7} involving multiple steps that can potentially introduce irregularities, defects, and weak interfaces between different material sections. For example, inflatable and pressure-driven structures, key components in soft robots, combine multiple materials with different moduli, elongations at break, and interfacial properties into complex structures (e.g., hollow structures such as pneumatic chambers),^{7–10} but sequential casting fabrication approaches can lead to

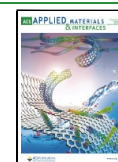
pneumatic failures due to weak interfaces, posing safety and performance issues. Additive manufacturing is a key alternative for enhancing multimaterial integration and interfacial bonding in soft robotics.^{5,11–13} The recent development of novel technologies, such as the combination of extrusion-based and digital-based printing techniques,^{14–17} enabled novel material combinations. The widespread use of support bath-based techniques could further enhance multimaterial integration, design freedom, and customization capabilities.

Various supporting media suitable for FL-3DP. The most popular are microparticle-based biopolymer hydrogels with jamming/unjamming behavior¹⁸ (e.g., Carbopol,^{19–23} gelatin,^{24–26} alginate,^{27,28} etc.), followed by polymer solutions with thixotropic properties (e.g., hyaluronic acid-based solutions,^{29,30} cellulose-based hydrogels,^{31,32} etc.), and underused

Received: October 19, 2021

Accepted: December 14, 2021

Published: December 28, 2021



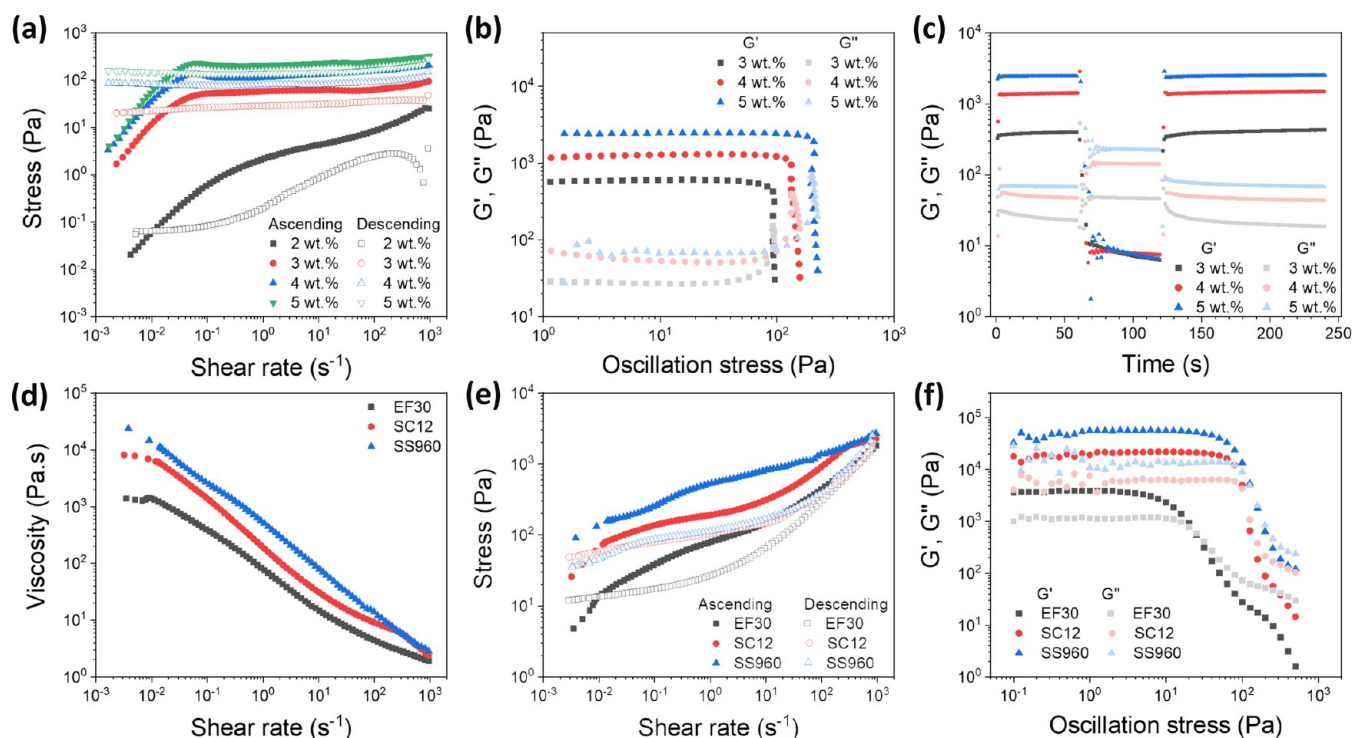


Figure 1. Rheological properties of Laponite-based hydrogels and silicone-based inks. (a) Stress versus shear rate as a function of Laponite concentrations obtained by steady shear measurement with ascending (solid markers) and descending (hollow markers) shear rates. (b) Storage (G') and loss (G'') moduli versus oscillation stress as a function of Laponite concentration obtained by oscillatory measurements. (c) Evolution of G' and G'' as a function of applied strain: a strain of 1% is applied for 60 s, followed by a strain of 100% for 60 s, ending with a strain of 1% for 120 s. (d) Viscosity versus shear rate for EF30, SC12, and SS960 obtained by steady shear. (e) Stress versus shear rate for EF30, SC12, and SS960 obtained by ascending (solid markers) and descending (hollow markers) steady shear. (f) Storage (G') and loss (G'') moduli versus oscillation stress obtained by oscillatory measurements.

mineral nanoparticle suspensions of Laponite nanoclay in aqueous supports^{33–37} or fumed silica in mineral oil.³⁸ Support media must display at least two key rheological properties: (i) a yield stress (σ_y) defining two states, with a liquid-like behavior above σ_y enabling a dispensing needle to move within the bath, and a solid-like behavior below σ_y needed to hold extruded features; and (ii) a short thixotropic time (usually <1 s), which is the time scale of the reversible transition between the solid-like and liquid-like behavior.

Inks reported in earlier studies were mainly hydrogel-based and suitable for tissue engineering applications, such as alginate,^{26,27,30,39,40} hyaluronic acid-based hydrogels,^{29,30,41,42} poly(vinyl alcohol) (PVA),¹⁹ etc. Few research teams have explored elastomers or polymers, with most reports solely focused on poly(dimethylsiloxane) (PDMS),^{19,20,28,43} epoxies,^{34,37,38} or polyurethanes.⁴⁴ These inks were used to fabricate various objects, ranging from basic structures such as shells,¹⁹ tubular networks and helices,^{20,21,33,34,37} and scaffolds and meshes,^{24,39,40,43} to more complex structures such as human organ-like structures.^{26,40} However, despite these numerous examples, the demonstration of advanced structures combining multiple materials with different functionalities is still lacking. Indeed, balancing the physicochemical properties between inks and supports to reduce instabilities, such as inertia, gravity, surface tensions, and viscosities, remains challenging but is required to avoid dragging or breakage of extruded features.^{2,23,45}

In this study, a FL-3DP approach was developed to process a wide range of room-temperature vulcanized (RTV) silicone-based inks. A nanoclay hydrogel was chosen as support for the

ease of synthesis, biocompatibility, low environmental impact, and recyclability. Both rheological properties and operational parameters were studied to better understand the filament morphology, thus enhancing printing resolution and enabling the precise combination of multiple inks. The enhancement of FL-3DP was demonstrated by designing advanced multi-material and pneumatic components for soft robotics applications. Soft grippers were chosen as an application example as this area is rapidly gaining traction to showcase the advantages offered by soft robotics.^{7,8,46,47} First, the high customizability enabled by FL-3DP was demonstrated through the design and fabrication of elastomeric sleeves that can be used to functionalize and tune standard (i.e., hard) or fabric-based pneumatic actuators (FPA).^{48,49} This approach augments gripping capabilities without the need to design an entirely new actuation platform. Second, the enhancement of component robustness compared to cast counterparts was demonstrated through the fabrication of an inflatable multi-material gripper palm that can be used with a variety of current soft actuators. The printed palm exhibited a longer lifespan under cycling conditions, by a factor of up to 13, compared to cast palms.

2. RESULTS AND DISCUSSION

2.1. Rheological Properties and Printability in FL-3DP.

2.1.1. Support Bath Properties. Support baths used in this study were obtained by dispersing Laponite nanoclay in deionized water (resistivity 18.2 M Ω). Laponite nanoparticles are inorganic silicate nanoplatelets (20 nm diameter and 2–4 nm thickness⁵⁰) arranged in a “house-of-cards” structure

Table 1. Rheological Properties of Support Baths^a

Laponite concentration (wt %)	static τ_y (Pa)	K (Pa·s ^{<i>n</i>})	n	TI _% (%)	G' (Pa)	tan δ
2.0	0.5 ± 0.1	1.1 ± 0.1	0.46 ± 0.01	88.5		
3.0	55.5 ± 0.6	0.5 ± 0.2	0.61 ± 0.06	52.2	600	0.05
3.5	47.3 ± 0.6	4.6 ± 0.5	0.29 ± 0.01	38.7	625	0.05
4.0	101.2 ± 1.3	14.3 ± 1.1	0.29 ± 0.01	43.2	1300	0.04
5.0	206.6 ± 1.8	5.7 ± 1.2	0.43 ± 0.03	32.5	2480	0.03

^aThe yield stress τ_y , the consistency index K , and the flow index n , were obtained by fitting the flow curves (see eq 1) with an ascending shear rate. The standard deviations were calculated from the fitting model. Storage and loss moduli were obtained in the solid-like behavior. Complementary information (i.e., fitting curves, dynamic yield stress, yield stresses from oscillatory experiments, R^2) is given in Sections S2 and S3.

through electrostatic interactions when dispersed in water. Surprisingly, only a few studies have reported Laponite as a support bath,^{34–37} despite its high versatility (thermal stability, UV and optical transparencies, biocompatibility) enabling a large range of curing mechanisms. Here, Laponite XLG (BYK additives, Southern Clay Products) was selected for its high purity and transparency.

The impact of Laponite concentration on the rheological properties of the support bath was studied by varying the concentration from 2 to 5 wt %. Both steady and oscillatory shear measurements were conducted to determine stress, storage (G'), and loss moduli (G''). Viscosities versus shear rates are reported in Section S1 and demonstrated an increase of the shear-thinning behavior (i.e., a decrease of viscosity with shear rate) with an increase in the Laponite concentration. Stress versus shear rates obtained by steady shear with ascending (solid markers) and descending (hollow markers) ramps are shown in Figure 1a. Thixotropic yield stress fluids can be characterized by two yield stresses:⁵¹ a dynamic yield stress corresponding to the minimum stress required to initiate the flow, and a static yield stress corresponding to the minimum stress to stop the flow. Both are crucial in FL-3DP as they describe the gel structuration and destructure dynamics and can be estimated by fitting the stress, τ (Pa), versus shear rate, $\dot{\gamma}$ (s^{−1}), curves with the Herschel–Bulkley (HB) model applied to the ascending and descending shear ramps, respectively

$$\begin{aligned}\tau &= \tau_y + K\dot{\gamma}^n, \quad \text{for } |\dot{\gamma}| > \tau_y \\ \dot{\gamma} &= 0, \quad \text{for } |\dot{\gamma}| < \tau_y\end{aligned}\quad (1)$$

where τ_y is the yield stress (Pa), n is the flow index (dimensionless), and K is the consistency index (Pa·s^{*n*}) related to the bath viscosity.⁵² Results of the fitting parameters for the ascending shear ramp are summarized in Table 1, while the fitting parameters for the descending shear ramp, the fitting curves, and the fitting coefficients (R^2) are reported in Section S2. As expected, the static yield stress increased with the Laponite concentration from 0.5 to ~200 Pa. The dynamic yield stresses for 2 and 3 wt % were extremely low and were not reached during the shear ramp-down experiments, suggesting that longer rest times are required for the reconstruction of the gel. Conversely, at 4 and 5 wt %, dynamic yield stresses were reached during the descending ramp, suggesting a faster restructure and thixotropic properties. This property was quantified through the thixotropic index (TI_%), or relative thixotropic area, defined as follows⁵²

$$\text{TI}_{\%} = \frac{(S_{\text{up}} - S_{\text{down}})}{S_{\text{up}}} \times 100 \quad (2)$$

where S_{up} and S_{down} are the areas under the ascending and descending flow curves, respectively. Here, the TI_%, given in Table 1, shows a significant decrease of the thixotropic behavior from 88 to 33% with the increase of Laponite concentration, confirming the less-time-dependent behavior at higher concentrations preferred for FL-3DP.

The evolution of storage (G') and loss (G'') moduli as a function of oscillation stress was determined by oscillation experiments with results shown in Figure 1b. All concentrations exhibited a solid-like behavior at low stress, with $G' > G''$ and values for G' increasing with the Laponite concentration from ~600 Pa to 2.5 kPa (see Table 1). Also, tan δ , defined as the ratio of the viscous response (G'') to the elastic response (G'), decreased with the increase of Laponite, supporting the higher gel elasticity observed in flow curves (see Figure S3). Above critical stress, G' sharply decreased and crossed G'' , marking a transition to a liquid-like behavior. As for flow experiments, static and dynamic yield stresses could be identified, corresponding respectively to the $G' - G''$ crossover point and the intersection of power-law fit of G' above and below the yielding point.⁵¹ Results confirmed the observations made by Dinkgreve et al. and are discussed in Section S3. The 2 wt % gel did not exhibit any solid-like behavior, with G'' well above G' for the entire stress range (shown in Figure S3).

Self-healing properties were assessed by conducting oscillatory measurements under a cyclic load: a low oscillation strain (1%) was applied for 60 s, followed by a high oscillation strain (100%) for 60 s, and concluded by a low oscillation strain (1%) for 120 s. The evolution of G' and G'' is shown in Figure 1c. For all concentrations, G' and G'' crossed at both changes within 1 s. For 4 and 5 wt %, G' recovered the value of the first cycle within 2 s, while ~10 s was necessary for the gel at 3 wt %. It should be noted that the oscillations observed at the beginning of the high-strain cycle were due to the stabilization time required for the rheometer to reach the prescribed strain (see Section S4). From these results, it was decided that a concentration of 3.5 wt % offered a good trade-off between the support and time scale recovery and was chosen for FL-3DP (the corresponding rheological properties and curves are reported in Table 1 and Sections S1–S3).

Unfortunately, there is a lack of references in the literature to compare these values. Laponite XLG used as a support bath was reported by Rodriguez et al.,³⁶ but only steady shear measurements were conducted and a concentration of 2.5% w/v was chosen to print silk fibroin. However, the authors coupled Laponite with poly(ethylene glycol) (PEG), thus increasing the viscosity at a low shear rate to facilitate the gelation of silk fibroin. Jin et al. studied other grades of nanoclay, i.e., Laponite EP^{33–35} and Laponite RD³⁴ used for general purpose and for high/low pH water-based systems, respectively. Yield stresses and storage moduli were lower than

Table 2. Rheological Properties of Inks^a

ink	static τ_y (Pa)	K (Pa·s ^{<i>n</i>})	n	TI ₀ (%)	G' (kPa)	tan δ
EF30	55 ± 10	30 ± 8	0.63 ± 0.03	29.6 ± 0.7	4.4 ± 0.5	0.29 ± 0.04
SC12	110 ± 20	32 ± 7	0.66 ± 0.01	47.0 ± 3.7	8.9 ± 0.7	0.31 ± 0.01
SS960	160 ± 40	155 ± 23	0.49 ± 0.03	42.0 ± 0.4	16.9 ± 2.5	0.25 ± 0.01

^aThe yield stress τ_y , the consistency index K , and the flow index n were obtained by fitting the flow curves with the ascending shear rate. The standard deviations were calculated from three samples. Storage and loss moduli were obtained in the solid-like behavior. Complementary information (fitting curves, dynamic yield stress, yield stresses from oscillatory experiments, R^2) is given in Sections S6 and S7.

the values reported here for a similar concentration, thus highlighting the need for more experiments on Laponite nanoclay support baths.

2.1.2. Ink Properties. In this work, three RTV silicone inks were selected to cover a wide range of stiffness and stretchability: (i) an extra-soft elastomer (Ecoflex 00-30, noted EF30, elastic modulus of ~70 kPa); (ii) a moderately-soft elastomer (Sorta-Clear 12, noted SC12, elastic modulus of ~240 kPa); and (iii) a stiff elastomer (Smooth-Sil 960, noted SS960, elastic modulus of ~1.9 MPa). A summary of the mechanical properties for the three cured materials is provided in Section S5. To improve the printability and pot life of the inks, a thickener (THI-VEX, Smooth-On) and a retardant (SLO-JO, Smooth-On) were added during the ink preparation (see Section 4 for details).

The rheological properties of the inks were determined by steady shear and oscillation measurements. Viscosity versus shear rate curves is reported in Figure 1d for EF30, SC12, and SS960. These inks exhibited shear-thinning behavior with the viscosity decreasing by 3 and 4 orders of magnitude for EF30 and both SC12 and SS960, respectively. Stress versus shear rate is shown in Figure 1e and static and dynamic yield stresses were determined by fitting the HB model to ascending and descending shear ramps (see Table 2 and Section S6). Static yield stresses were higher than dynamic yield stresses for all inks, and EF30 exhibited the lowest yield stress (55 Pa) compared to SC12 (110 Pa) and SS960 (160 Pa). As seen from the hysteresis between the ascending and descending shear rate, the inks exhibited a similar thixotropic behavior: the TI₀ was ~30% for EF30 and ~45% for SC12 and SS960 (see Table 2). These results were confirmed by oscillatory measurements reported in Figure 1f: the lowest yield stresses (static and dynamic) and elastic modulus were obtained for EF30 (~25, ~15, and ~4 kPa, respectively), while SS960 exhibited the highest yield stresses (~75 and ~52 Pa for static and dynamic yield stresses) and storage modulus (~17 kPa).

2.1.3. Filament Characterization. In FL-3DP, the ink is loaded into a syringe dispenser that can be fitted with various hypodermic needle sizes. Inks are extruded by controlling the air pressure, P_0 , applied to the syringe plunger using a pressure controller (Nordson). Moving the needle within the support bath induces a strong gradient of shear (high shear around the needle, lower shear away from the needle, see Figure 2a), resulting in a yielded fluid envelope with localized liquefaction of the support bath. The size of this envelope can impact the ink distribution behind the needle and thus the filament shape, as illustrated in Figure 2b,c. The Oldroyd number, Od , (ratio of the bath yield stress to the viscous stresses in a flow) can be used to evaluate the size of the yielded fluid envelope around a cylinder⁵³

$$Od = \frac{\tau_y D_o^n}{KV_N^n} \quad (3)$$

where τ_y , K , and n are the coefficients of the HB model of the bath (see Table 1); V_N is the translational speed of the needle; and D_o is the outer diameter of the needle. By using particle image velocimetry to determine the yielded area, Grosskopf et al. showed that increasing the Od number (by increasing τ_y or D_o , or decreasing V_N) reduces the yielded area, thus improving the print fidelity.⁵³

Here, the impact of operational conditions on the filament shape was studied by printing horizontal lines (20 mm) by varying the pressure, P_0 , and the horizontal speed of the needle, V_N , while using an identical stainless steel needle (inner diameter $D_N = 0.66$ mm and length $L_N = 38.1$ mm) for the three inks (see Figure 2d). After extrusion, the filaments were measured within the bath using an optical microscope (Hirox), and the horizontal plane diameter, d_{fl} , (i.e., the filament thickness in the horizontal plane) was plotted against V_N and P_0 (see Figure 2e). For a given input pressure, the diameters of all inks decreased with the increase of the needle velocity following a negative square root law.

After curing, the filaments were cut, and the cross sections were observed under an optical microscope (KH-8700, Hirox). As seen from the insets in Figure 2e, EF30 filaments exhibited strong tear-shaped cross sections at low speed and high pressure, while SC12 and SS960 had oval cross sections. Reducing the pressure and increasing the speed reduced the oval shape for all inks, with SS960 cross sections overall more circular than SC12 and EF30 for all conditions. This was further quantified by approximating the cross sections to an ellipse and measuring for all filaments the minor (d_{fl}) and major (d_{fl2}) diameters (i.e., the horizontal and vertical thicknesses, respectively). The eccentricity e ($e = \sqrt{1 - d_{fl}^2/d_{fl2}^2}$) was then calculated and reported in Figure 2f. Increasing needle speed and decreasing pressure reduced the eccentricity. The reduction with speed was clearer at lower pressures. For example, the eccentricities of EF30 and SC12 extruded at 14 kPa reduced from ~0.85 to ~0.2 and to ~0.4, respectively. At higher pressures, the eccentricities decreased first before reaching a plateau for speeds above 5–7.5 mm·s⁻¹.

The observed trends were expected, as the filament shape is controlled by both the ink flow rate and the support yielded area. Decreasing the flow rate (by decreasing the pressure or increasing speed) reduces both d_{fl} and e , as less ink is extruded. Increasing the yielded area (by increasing the needle speed as expressed in the Od number) decreases e , as the ink is less constrained by the nonyielded support when extruded (see Figure 2b). The unexpected stabilization of e for EF30 and SC12 at higher pressures (41, 55, and 61 kPa) suggested that the yielded area was not large enough compared to the flow rate of the ink.

In addition to needle speed, the yielded area is also governed by the yield stress of the support. This was confirmed by conducting a similar study with a stiffer bath (4.5 wt %

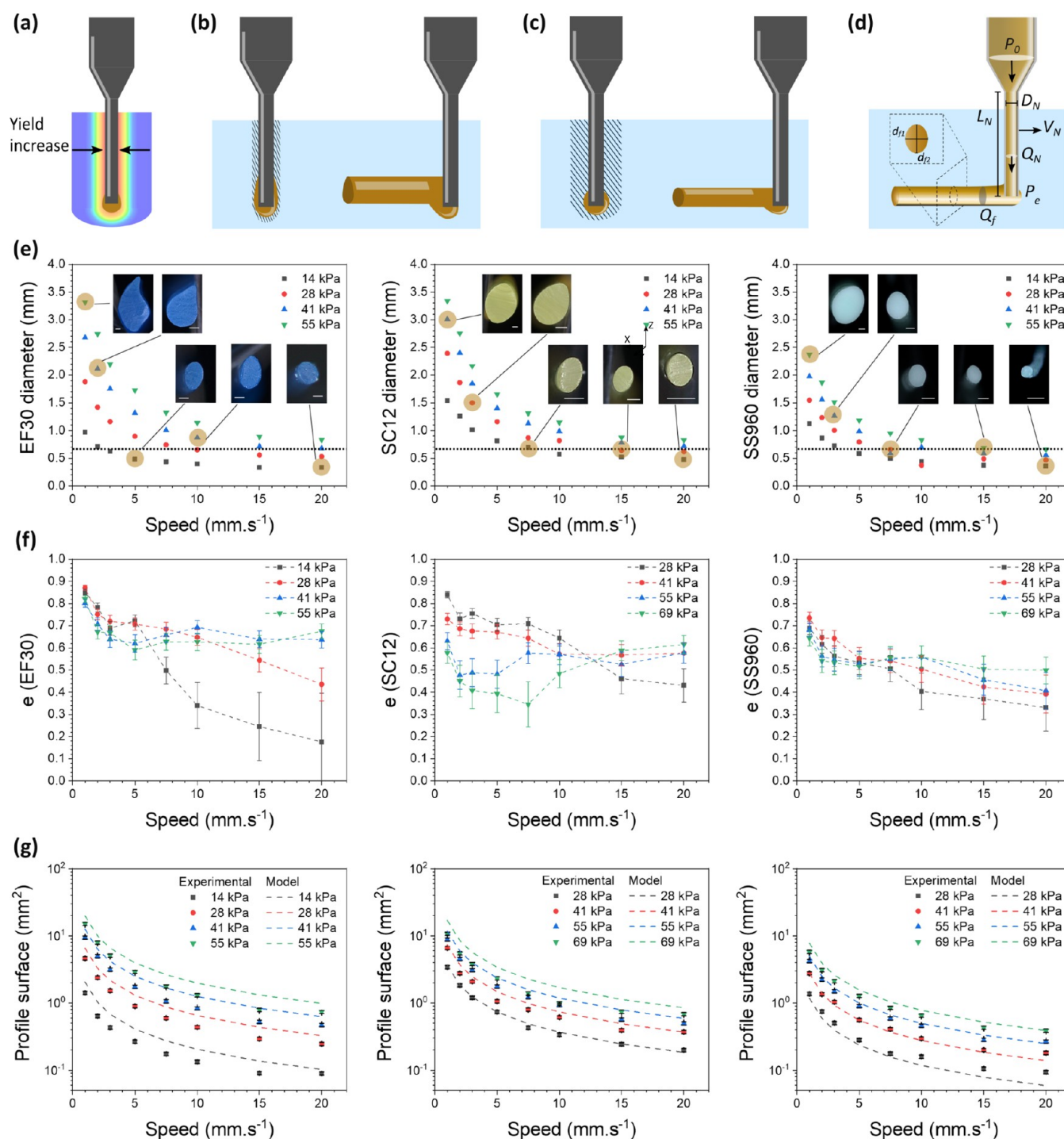


Figure 2. Impact of printing parameters on filament dimensions. (a) Illustration of the qualitative stress distribution around a cylinder moving inside the support (front view). (b) Schematic front and side views of filament extrusion inside a support with a narrow yielded fluid envelope (represented by the dashed area): the narrow area tends to squeeze the filament into a tear-shaped or ellipse-shaped cross section. (c) Schematic front and side views of filament extrusion inside a support with a large yielded fluid envelope (represented by the dashed area): the filament has a more circular cross section. (d) Model parameters. (e) Impact of the input pressure and needle speed on filament diameters and cross sections (extrusion using a needle of an inner diameter of 0.66 mm, represented by a horizontal dashed line). Insets show optical microscope pictures of some of the cross sections (scale bar represents 500 μm). (f) Eccentricity of the cross sections obtained from the minor and major diameters. The deviations were calculated by propagation of uncertainties. (g) Comparison between filament cross-sectional surfaces measured through experiments (assumed as ellipses) and model predictions.

concentration), detailed in Section S8. The decrease of the yielded area and the subsequent increase of e were confirmed for all inks with unequal impacts: the eccentricities of EF30 were significantly increased (to 0.8–0.9 for most pressures),

while the eccentricities of SS960 increased less significantly (up to 0.6–0.7). This illustrates the importance of balancing the bath yield stress according to the printed ink rheological properties.

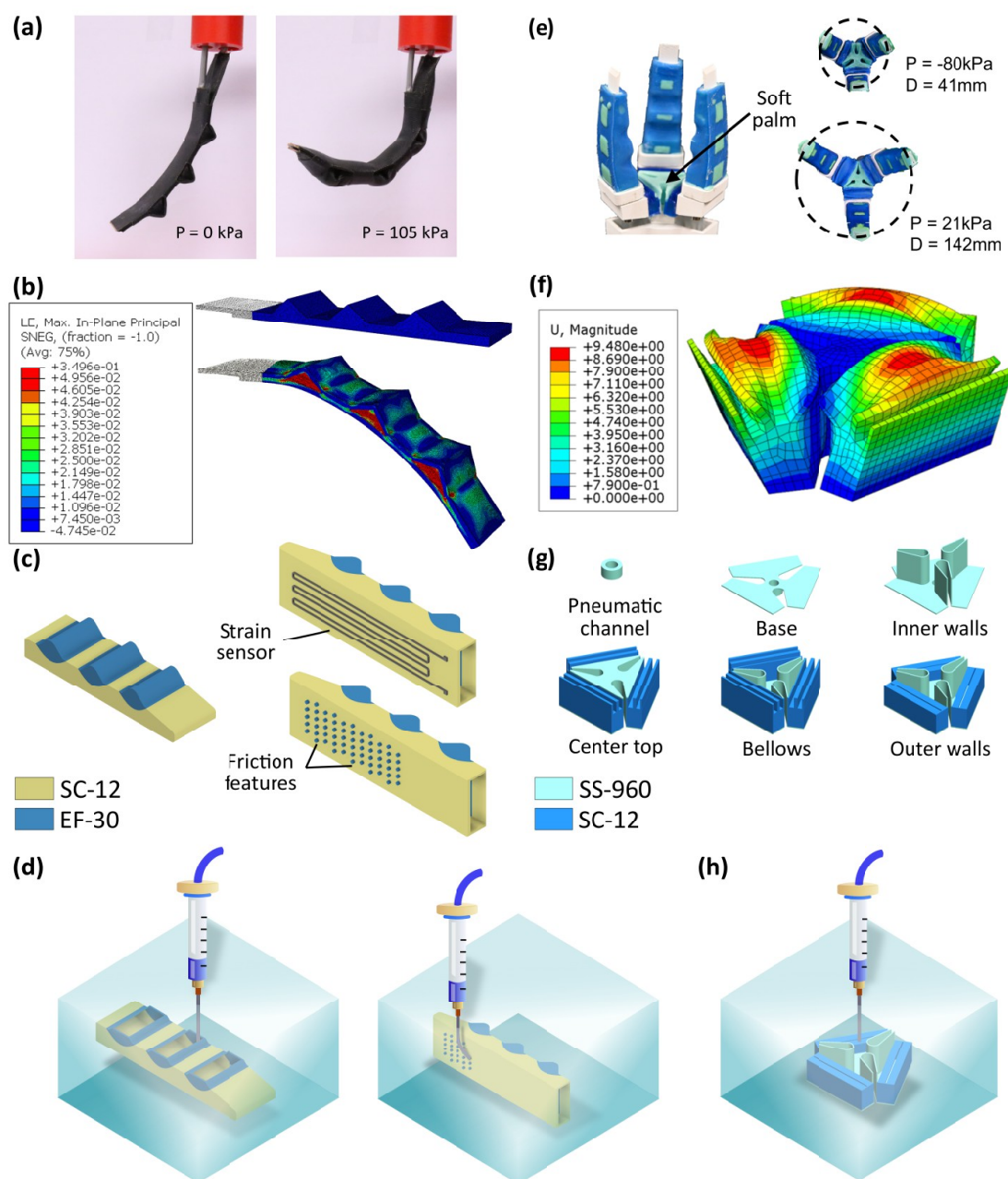


Figure 3. Design and fabrication approach of soft multimaterial functional components. (a–d) Design and fabrication of customized functional sleeves for fabric-based grippers: (a) Fabric-based pneumatic actuator (FPA) before and after actuation at 105 kPa; (b) finite elemental analysis (FEA) of an FPA-like structure dressed with a soft sleeve (EF30) actuated at 28 kPa showing the strain distribution concentrated around the phalanges; (c) design of multimaterial sleeves based on FEA: sensorized sleeves have an embedded strain sensor and textured sleeves have multiple pillars on the gripping surface; (d) illustration of the two printing orientations chosen according to the additional functional features (the strain sensor could be printed in both orientations). (e–h) Design and fabrication of an inflatable gripper palm: (e) pictures of the complete gripper, which includes three soft fingers and the inflatable palm to control the gripper aperture; (f) FEA of the palm showing the expansion of the bellows when actuated at 20 kPa; (g) design of the palm components; and (h) illustration of the palm FL-3DP.

Besides these parameters, the buoyancy of the ink could also have an impact on the filament. The use of a support enables efficient stabilization of the ink once printed, as long as the gravitational forces are lower than the yielding force (expressed as $\Delta\rho Vg < \sigma_f A$, where $\Delta\rho$ is the density difference between the ink and support, V is the volume of printed ink, g is the gravitational constant, and A is the hydrodynamic surface area).⁴⁵ However, during the print, considering that the whole area behind the needle behaves as a liquid, the ink density

might impact the height at which the filament stabilizes behind the needle. This will be assessed in future studies.

2.1.4. Estimation of Filament Geometries. Due to the number of parameters and physical phenomena involved, building mathematical models to predict the filament shapes described in the previous section is challenging. However, estimations can be done from the rheological properties of both inks and supports^{54,55} and an approximate model is described herein. First, several assumptions were made: (i) the materials were assumed to be homogeneous, isotropic,

incompressible, and in steady-state laminar flow; (ii) a no-slip condition was assumed on the surface of the needle; (iii) friction losses were neglected; and (iv) gravitational forces were neglected due to the high pressures applied in the syringe. The model inputs include the dispenser pressure, P_0 , and the needle horizontal speed, V_N . The needle inner diameter D_N and length L_N were assumed to be constant (parameters chosen by the user and motivated by the dimensions of the object to print). For simplification, as the cross section of the filament is not spherical, the model output is the surface, S , of the cross section, assumed to be elliptic with minor, d_{f1} , and major, d_{f2} , diameters (see Figure 2d)

$$S = \pi d_{f1} d_{f2} = f(P_0, V_N) \quad (4)$$

The ink flow rate Q_N at the exit of the needle (in the presence of an external pressure P_e , see Figure 2d) can be calculated with the following equation using the ink HB model (i.e., σ_y , K , and n)^{54,55}

$$Q_N = \pi \frac{D_N^3}{8} \cdot \left(\frac{(P_0 - P_e) D_N}{4KL_N} \right)^{1/n} \cdot \frac{4n}{(3n + 1)} \cdot (1 - X)^{1/n} \cdot (1 - aX - bX^2 - cX^3) \quad (5)$$

where X is given by

$$X = \frac{4L_N \tau_y}{D_N(P_0 - P_e)}$$

and the coefficients a , b , and c , are given by

$$a = \frac{1}{(2n + 1)}, \quad b = \frac{2n}{(n + 1)(2n + 1)}, \quad c = \frac{2n^2}{(n + 1)(2n + 1)}$$

From mass conservation, Q_N should be equal to the flow rate Q_f of the extruded filament with an ellipse-like cross section

$$Q_N = Q_f = SV_N = \pi d_{f1} d_{f2} V_N \quad (6)$$

Combining eqs 5 and 6, S can be expressed as a function of the input pressure, P_0 , and horizontal needle speed, V_N , as follows

$$S = \frac{\pi D_N^3}{8V_N} \cdot \left(\frac{(P_0 - P_e) D_N}{4KL_N} \right)^{1/n} \cdot \frac{4n}{(3n + 1)} \cdot (1 - X)^{1/n} \cdot (1 - aX - bX^2 - cX^3) \quad (7)$$

The support bath is expected to have a negligible effect on the mass conservation stated above. For simplification, P_e can be assumed to be equal to the yield stress of the bath ($\sim 10^2$ Pa), thus negligible compared to P_0 ($> 10^5$ Pa).³³ In addition, the bath's hydrostatic pressure, ρgh (where ρ is the density of the fluid, g is the acceleration constant, and h is the height of the bath) is also negligible (10^2 – 10^3 Pa for prints of 1–10 cm height), leading to a simplified equation

$$S = \frac{\pi D_N^3}{8V_N} \cdot \left(\frac{P_0 D_N}{4KL_N} \right)^{1/n} \cdot \frac{4n}{(3n + 1)} \cdot (1 - X)^{1/n} \cdot (1 - aX - bX^2 - cX^3) \quad (8)$$

The model was assessed by comparing the surface measured experimentally (by assuming an ellipse shape, with d_{f1} and d_{f2} reported in Figure 2d–f) and the surface calculated from eq 7.

The resulting curves are reported in Figure 2g. The model predictions were larger than the values found experimentally for EF30 at all pressures, with errors ranging from 10 to 40%. The model predictions were more accurate for SC12 at low pressures (error up to 10%), but the error increased to 20–30% at higher pressures. For SS960, the model slightly overestimated the surfaces but was globally within the range (error of 10–25%). Overall, the errors were observed at high pressures for filaments with a tear-shaped cross section (see Figure 2e), where the assumption of an elliptic cross section could underestimate the surface. For filaments with a more spherical or elliptic cross section, the model described well the flow of the ink. Improving the model further will require a better assessment of both the filament shape and the yielded area that could be estimated from the Od number and will be the subject of future studies.

2.2. Design and Fabrication of Functional Soft Components. 2.2.1. Design.

The two soft functional devices are shown in Figure 3. First, a bidirectional FPA was chosen as the base of a hybrid pneumatic gripper for its ease of fabrication, low-form factor, and large resistive gripping forces.⁴⁸ The actuator consists of two pneumatic textile layers bonded together, one straight and the other folded to form phalanges (see Figure 3a). A finite element analysis (FEA) on the FPA was performed to identify areas with large strain deformations during actuation (Figure 3b). A dual-material sleeve was designed accordingly, combining EF30 and SC12 for regions with large or limited strains, respectively (e.g., around the phalanges) to maintain a tailored fit of the sleeve around the textile actuator (see Figure 3c). This design was further functionalized through two separate enhancements: (i) a strain sensor made of carbon grease was embedded inside the gripping face of the sleeve to provide feedback on the bending state of the actuator as well as contact forces; and (ii) the gripping face of the sleeve was textured with mini pillars made of either stiff (SS960) or soft (EF30) elastomers to tune the surface friction properties. A different printing orientation strategy, illustrated in Figure 3d, was used for each configuration (i.e., sensorized sleeves or textured sleeves (TS)). After curing (~ 24 h in ambient temperature or less than 2 h at 80 °C), the support is simply washed-off and the sleeves can be mounted on the FPA. Finally, the strain sensors were connected via flexible fiber interconnects (FFI, see ref 56 for details) for signal recording.

The second example consists of a bidirectional multimaterial pneumatic palm actively controlling a gripper's aperture (see Figure 3e). The trefoil-shaped palm, as shown in Figure 3f,g, is hollow and consists of three sides with soft inflatable bellows (SC12) connected to a stiffer center (SS960). By applying positive or negative pressure to the palm, the inflatable bellows and sides expand or collapse, causing the gripper aperture to increase or decrease, respectively. The palm FL-3DP, as shown in Figure 3h, enables the incorporation of multiple materials to achieve the desired palm kinematics.

2.2.2. Fabrication. Determining the filament shape, as described in Section 2, is critical for successful FL-3DP as variations in the filament shape can lead to weak bonding or even gaps between layers and phases, which can severely affect the performance.¹² The characterization of the elliptical cross section coupled with the identification of different behaviors among the inks enabled adjustments to the slicing of STL files and resulted in more precise prints. In particular, the strong eccentricity of EF30 imposed more space between lines in the

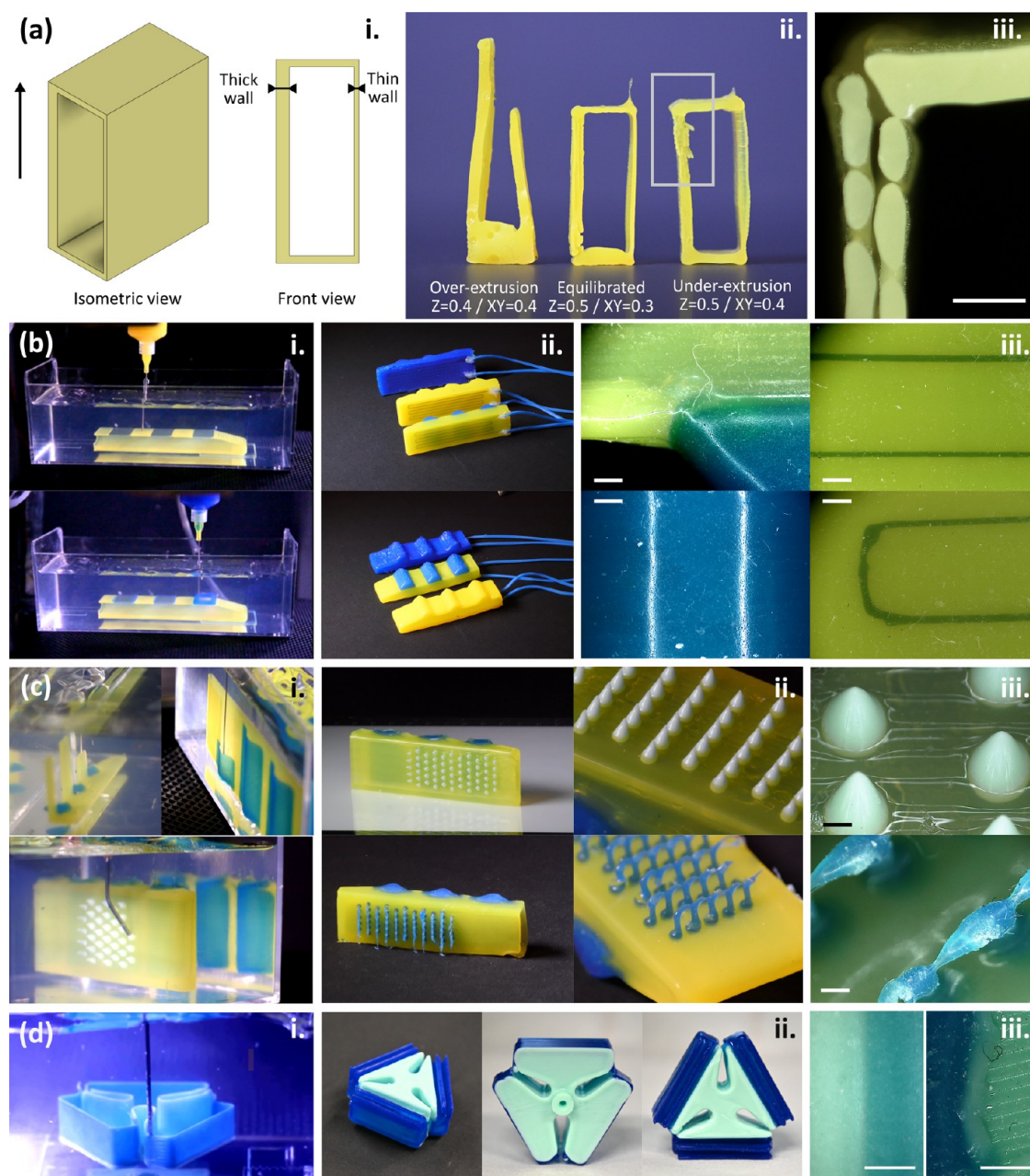


Figure 4. Freeform liquid 3D printing of soft multimaterial components. (a) Illustration of the impact of the filament morphology on required printing parameters: (i) Computer-aided design (CAD) drawing of an asymmetric rectangular shape, with a thick wall (2 mm) requiring three lines and a thin wall (0.6 mm) requiring only one line (the arrow indicates the printing direction); (ii) printed rectangular shapes with different slicing parameters for the Z-direction and the XY-plane; (iii) close-up view of the partial fusion of filaments printed for the under-extruded rectangle (scale bar corresponds to 2 mm). (b) (i) FL-3DP of the functional composite sleeve; (ii) three functional sleeves wired with flexible fiber interconnects (EF30 in blue and SC12 in yellow); (iii) Microscopy images of the functional composite sleeve highlighting excellent fusion at the interface of the two phases, smooth surfaces due to excellent layer fusion, and the conductive path of the strain sensor (scale bar corresponds to 1 mm). (c) (i) FL-3DP of the textured composite sleeve; (ii) composite sleeves with SS960 and EF30 pillars; (iii) microscopy image of the features embedded on the sleeve (scale bar corresponds to 1 mm). (d) (i) Multimaterial palm FL-3DP (SC12 in blue and SS960 in green); (ii) various views of the printed palm; and (iii) microscopy image of the interface between SC12 and SS960 on a printed (left) and cast (right) palm (scale bar corresponds to 0.5 mm).

Z-direction than for SS960. This was illustrated in Figure 4a, where the same asymmetric rectangular shape (one thick wall requiring three lines, and one thin wall requiring one line) was printed in EF30 with different slicing parameters. In over-extrusion conditions, the rectangular shape could not be printed, as the base was severely deformed and the thick wall was much higher due to the accumulation of inks in the Z-direction. In under-extrusion conditions, the layers were fused

in the Z-direction, but not in the XY-plane, resulting in a thick wall divided into filaments. By adjusting the layering in the Z- and XY-directions, proper fusion could be obtained in all directions.

The operational parameters for the three inks were adjusted to minimize ϵ and to obtain d_{fl} values close to D_N . All prints were conducted with a 20-gauge needle (McMaster, 0.66 mm inner diameter and 38 mm length) with a horizontal speed

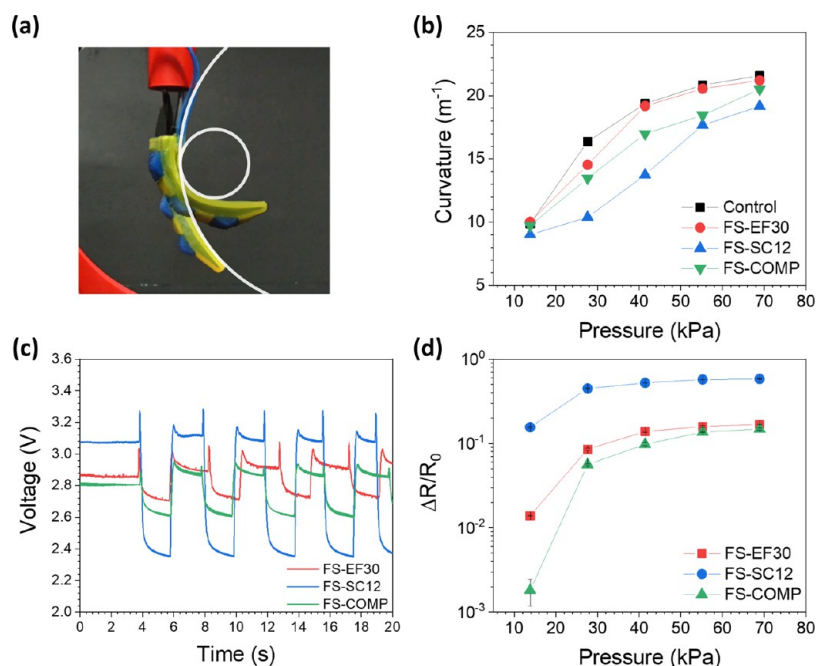


Figure 5. Bending characterization of the functional sleeves. (a) Overlaid image illustrating the bending of the composite sleeve under pressure actuation (70 kPa) and measurement of the change of the curvature. (b) Impact of the actuation pressure on the soft (FS-EF30), stiff (FS-SC12), and composite (FS-COMP) sleeve-measured curvatures. (c) Voltage versus time measured for all sleeves actuated for 2 s at 70 kPa, repeated five times. (d) Sensitivity of the strain sensor for the three sleeves.

ranging from 5 to $10 \text{ mm} \cdot \text{s}^{-1}$. First, three sleeves (noted FS) were functionalized by embedding strain sensors (see Figure 4b): (i) a soft monomaterial sleeve made of EF30 (blue, noted FS-EF30); (ii) a stiff monomaterial made of SC12 (yellow, noted FS-SC12); and (iii) a composite combining both materials (noted FS-COMP). Sleeves were printed horizontally, first the base, followed by embedding of the strain sensor, and finally printing the walls and top (see Movie S1). After curing, the sleeves were removed from the support, washed with DI water, and dried at ambient temperature. The strain sensor was then connected using flexible fiber interconnects (FFI)⁵⁶ for easy plugging to a data acquisition unit. Finally, microscopy pictures highlight the high quality of the prints: layers were fully fused, the strain sensor was embedded, and interfaces between materials were smooth (see Figure 4b-iii).

Textured composite sleeves (noted TS) with pillars were also printed (see Figure 4c). The printing orientation was modified to easily extrude pillars using bent needles (45° angle, 0.97 mm inner diameter, 25.4 mm length). Two types of pillars were printed: stiff pillars made of SS960 (noted TS-SS960) and highly soft pillars made of EF30 (noted TS-EF30). As the orientation changed, the sequence of printing was also modified: SC12 and EF30 inks were alternatively printed in each of the three sleeve sections (see Movie S2). Strain sensors were not printed on the TS to minimize printing time, but one could easily add a strain sensor before extruding the pillars if required. Both TS-SS960 and TS-EF30 are shown in Figure 4c along with microscopy images of the pillars.

Finally, the FL-3DP of the multimaterial palm is shown in Figure 4d. First, SS960 was extruded to fabricate the base of the central structure, followed by SC12 to build the inflatable bellows (see Movie S3). The fully printed palm is shown, and optical micrographs revealed again a smooth interface between the two materials, unlike the cast palm version where phase separation at the interface is clearly visible.

2.3. Sleeve Characterization. **2.3.1. Bending and Functionality.** After curing, the sleeves were characterized in terms of bending curvature and sensor functionality. The actuator was mounted on a custom-made support connected to a pressure dispenser (Nordson), dressed with the sleeves, and connected to a data acquisition unit (National Instruments). An increasing pressure from 15 to 70 kPa was applied to the actuator. First, the change of curvature was measured using open-source software ImageJ (see Figure 5a) and reported in Figure 5b. Without the sleeve (control setup), the curvature increased with pressure, from ~ 10 to $\sim 21 \text{ m}^{-1}$. Similar curvatures were obtained with the softest sleeve (FS-EF30), while the stiffest sleeve (FS-SC12) exhibited lower curvatures for all pressures, increasing from only ~ 9 to $\sim 19 \text{ m}^{-1}$. The composite sleeve (FS-COMP) obtained closer values to FS-EF30, validating the relevance of the design in the composite sleeve. Furthermore, the differences between the sleeves were less visible at high pressures ($>70 \text{ kPa}$), suggesting the possibility of overcoming the bending restrictions not only by increasing the pressure but also by increasing the risk of actuator failure.

The embedded sensors act as a resistance whose value changes with structural deformations. These changes in resistance are gauged by measuring the voltage across the sensor resistance using a voltage divider circuit. By recording the change of voltage during actuation for five cycles at 70 kPa (see Figure 5c), the sensitivity of the embedded sensors could be assessed. A similar pattern was observed for the three sleeves, with two plateaus clearly distinguishing the actuated and nonactuated states. Variations in the thickness and depth of the embedded sensors were noticed, challenging a clear interpretation of absolute voltage values. These variations were due to the conductive ink preparation and remaining manual operations, such as the change of syringe and visual calibrations. This could be improved by further work on

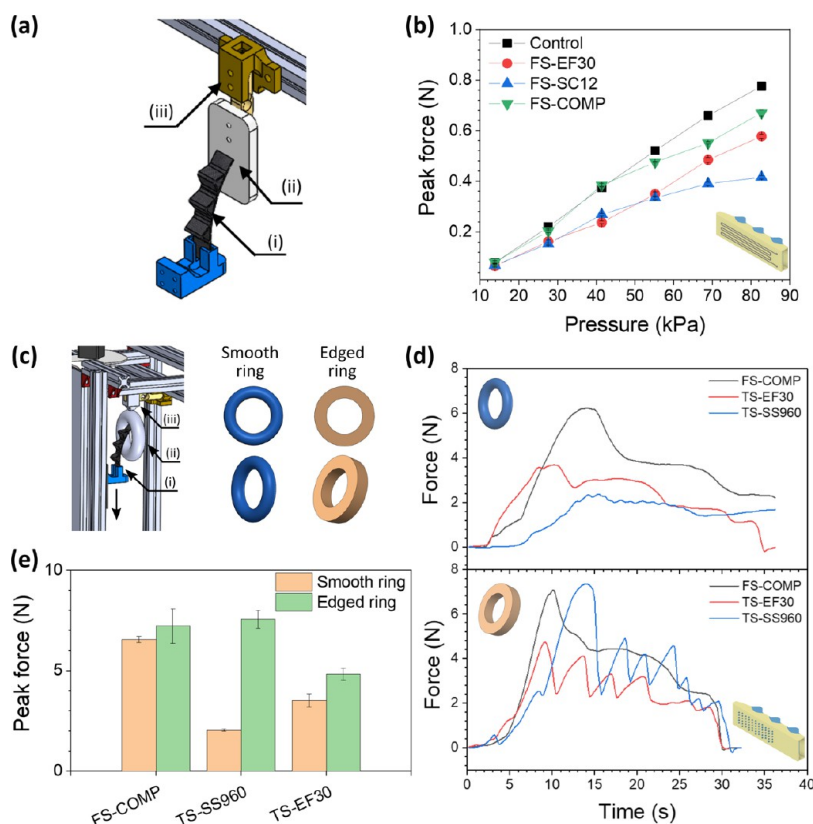


Figure 6. Tuning the gripping capabilities of a fabric-based actuator. (a) Illustration of the blocking force experiments: (i) fabric-based actuator with a sleeve, (ii) 3D-printed plate mounted on (iii) load cell (50 N capacity). (b) Evolution of the normal forces as a function of actuation pressure. (c) Illustration of the unwrapping experiment: (i) fabric-based actuator with the sleeve is mounted on a movable stage and actuated; (ii) a ring is mounted on (iii) the load cell and the force exerted by the actuator on the ring is recorded. Two rings were used: a smooth surface ring and an edged surface ring. (d) Impact of the sleeve texture on the unwrapping force of the actuator (at 80 kPa) on the smooth (top panel) and edged (bottom panel) rings. (e) Resulting peak forces during the unwrapping tests.

both hardware development and formulation of more stable conductive inks. In an attempt to still compare the sensitivity between different sleeves, the relative change of resistance between the actuated (R) and the nonactuated (R_0) states was calculated by the ratio $(R - R_0)/R_0$ (denoted as $\Delta R/R_0$), reported in Figure 5d. The sleeve FS-SC12 exhibited the highest ratio but the slowest increase with applied pressure, with a ratio rapidly converging from ~ 0.15 to ~ 0.6 for pressures above 27 kPa. This can be explained by the stiffness of SC12, which induces more stress on the sensor, while the low increase with pressure can be explained by the poor bending capability described in Figure 1b. In comparison, FS-COMP exhibited the highest change of resistance with the applied pressure: the ratio increased by about 2 orders of magnitude, from ~ 0.002 to ~ 0.15 when increasing the pressure from 10 to 80 kPa, demonstrating the good deformability of the sleeve coupled with a higher sensitivity of the sensor embedded in stiff SC12. Though, it should be noted that strain sensors made of carbon grease display time-dependent behavior,⁵⁷ and the use of more stable strain sensors will be explored in future studies.

2.3.2. Tuning Gripping Capabilities. The gripping capabilities of fabric-based pneumatic grippers equipped with the sleeves were assessed through two experiments. First, an actuator tip-block force test, illustrated in Figure 6a, was used to measure the normal force exerted by the functional sleeves (FS) on a plate attached to a load cell (50 N capacity, Sparkfun TAL220B). The peak forces measured during the test were

recorded as a function of actuator pressure and results, averaged from five tests, are shown in Figure 6b. The control experiment (no sleeve) exerted the highest normal force (0.8 N), as the sleeve did not constrain the bending of the actuator. With the sleeves, the peak forces were lower, the soft and stiff sleeves reaching 0.57 and 0.42 N, respectively. Interestingly, the peak force obtained with the composite was much higher than both monomaterial sleeves, with values close to the control and reaching a maximum of 0.67 N at 83 kPa. This can be explained by two phenomena: (i) the lower constrain exerted by FS-COMP compared to FS-SC12 (see the curvature in Figure 5b); (ii) the higher force exerted by FS-COMP compared to FS-EF30 due to the use of a stiffer (i.e., less viscoelastic) SC12 in the grasping surface of the sleeve.

Second, an unwrapping test, shown in Figure 6c, was conducted with the actuator mounted on a moveable stage and actuated using an input pressure of 83 kPa to hook grasp a ring fixed to a 50 N load cell (Sparkfun Inc.). The stage was then moved down at a constant speed of $5 \text{ mm} \cdot \text{s}^{-1}$, causing the actuator to unwrap and release the ring while the forces exerted by the actuator on the ring were measured (see Movie S4). To simulate different grasping scenarios involving smooth and rough payloads, two custom-made rings in acrylic-styrene-acrylonitrile (ASA) were used: a toroid-shaped ring with a smooth surface and a cylindrical ring with an edge (see Figure 6c). The first set of measurements were made with the functional sleeves (i.e., without pillars), and the results are reported in Section S9. Briefly, the results were similar to the

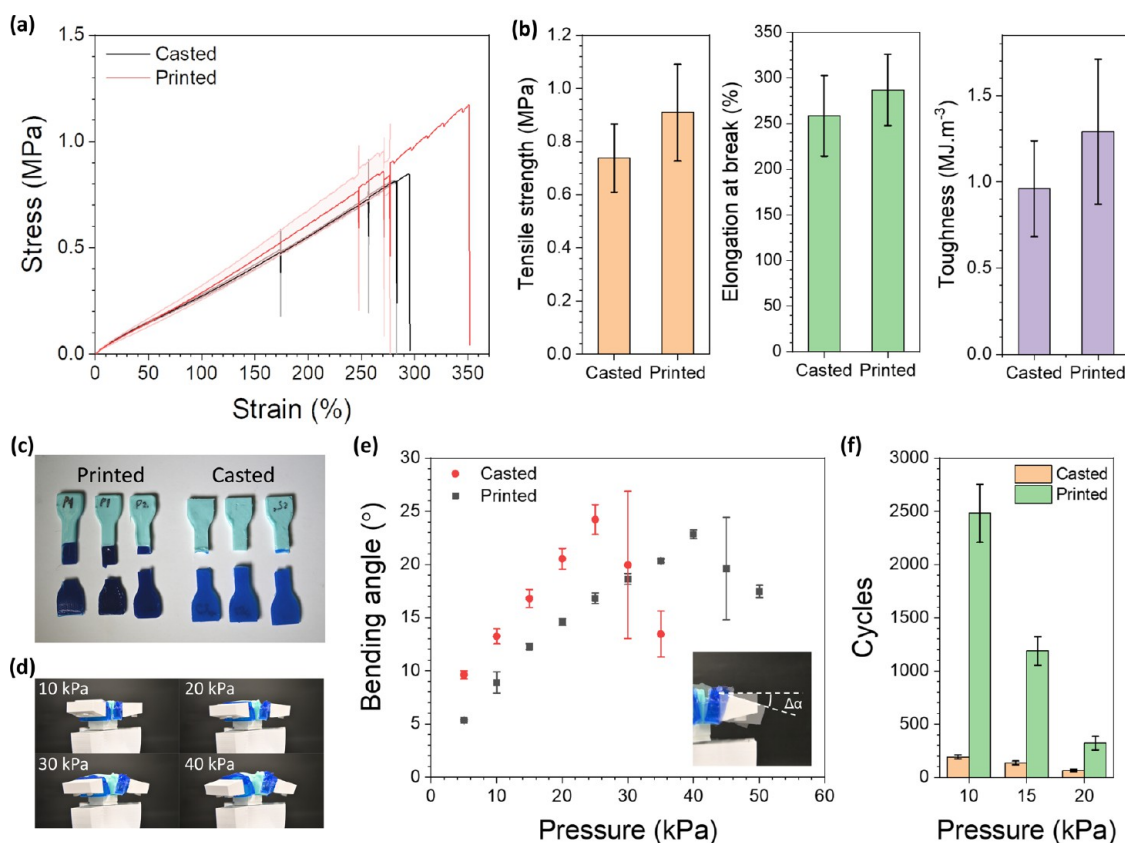


Figure 7. Characterization of a multimaterial inflatable palm. (a) Tensile test of the cast and printed multimaterial tensile specimens (SC12/SS960) averaged from five samples. (b) Tensile strength, elongation at break, and toughness measured for cast and printed multimaterial tensile specimens averaged from five samples. (c) Picture illustrating the location of the crack: within the soft SC12 region for printed samples and at the interface for cast samples. (d) Picture showing the inflation of the palm when increasing the input pressure from 10 to 40 kPa. (e) Comparison of the bending angle (defined in the inset) between the cast and printed palms as a function of applied pressure. (f) Number of inflation/deflation cycles before failure for printed and the cast palms (input pressures of 10, 15, and 20 kPa).

block test: FS-COMP and FS-EF30 displayed a higher wrapping force than FS-SC12, thus again supporting the relevance of the composite design. Interestingly, the sleeves enhanced by a factor of 3 the unwrapping force compared to the neat fabric-based actuator, as the coefficient of friction of silicone rubbers (naturally tacky) on ABS can be assumed higher than textiles.

The second set of experiments was conducted on the textured sleeves (TS). Three composite sleeves were compared: nontextured FS-COMP (with no pillars), TS-EF30 (with soft pillars), and TS-SS960 (with stiff pillars). The corresponding curves are shown in Figure 6d for both smooth (top panel) and edged (bottom panel) rings, and the maximum forces are compared in Figure 6e. On a smooth ring, the use of pillars greatly decreased the maximum unwrapping force obtained, with only 2.0 and 3.5 N for TS-SS960 and TS-EF30, respectively, to be compared with 6.5 N for nontextured FS-COMP. This can be explained by a reduction of the contact area between the sleeve and the ring, concentrated at the tip of the pillars. This phenomenon is less pronounced for EF30 pillars, as they are more deformable and thus have better contact surface areas. On an edged surface, repeated force peaks were identified for both textured sleeves, while FS-COMP exhibited a single peak. These peaks were due to the hooking of the pillars on the ring surface. As a result, the contact surfaces were improved, giving a maximum force of ~7.5 N with TS-SS960, as the stiff pillars could support a

higher force than the soft pillars before deformation. Overall, these results show how the gripping forces and functionality can be tuned by easily customizing the functional sleeves using FL-3DP.

2.4. Characterization of a Multimaterial Inflatable Palm. The second example illustrates how FL-3DP can enhance the interfacial toughness across phases compared to traditional casting. Performances and the lifespan of printed and cast multimaterial palms were compared. Due to the complex geometry of the palm, casting required sequential fabrication; the first cast material needed to be cured before casting the second material. This resulted in several mold preparations, casting, and demolding steps illustrated in Section S10, which invariably resulted in a longer fabrication time and introduction of defects due to manual mold assembly errors, damage of thin walls and delicate structures during demolding, and contamination of the interfaces between casting steps. Alternatively, FL-3DP provided an automated approach, reducing fabrication time and allowing for all materials to be processed simultaneously, forming stronger interfaces between materials during curing.

A first qualitative test was conducted by comparing tensile tests of cast and printed multimaterial tensile test specimens made of SC12 and SS960 (10 mm × 15 mm × 4 mm each side) up to rupture. To reproduce the casting conditions of the palm, the cast specimens were fabricated sequentially (i.e., curing SC12 before casting SS960). The stress versus strain

curves averaged from five samples each are reported in Figure 7a, with the corresponding tensile strengths, elongations at break, and toughness reported in Figure 7b. The printed samples exhibited slightly higher values than cast samples (~ 0.9 versus ~ 0.7 MPa, ~ 290 versus $\sim 260\%$, and ~ 1.3 versus ~ 0.9 MJ·m $^{-3}$ for tensile strength, maximum elongation, and toughness, respectively). More importantly, as seen in Figure 7c, the cast samples failed at the interface (i.e., adhesive fracture mode), while the printed samples failed within the softest component SC12 (i.e., cohesive fracture), suggesting that casting introduced more weaknesses at the interface than FL-3DP. This can be explained by sequential casting: by curing one material after the other, the reticulation at the interface is not as strong as when the two phases cure simultaneously.¹²

This difference in interfacial toughness impacted the performance of the palms. First, the actuation of the palm was studied as a function of input pressure: the palm was inflated at a steady pressure for 3 s, as seen in Figure 7d, and the palm side bending angle ($\Delta\alpha$) was measured (see Figure 7e). The pressure was increased by an increment of 5 kPa until failure of the palm. The results, averaged from three palm prototypes, show that the printed palms could withstand higher pressures (40 versus 25 kPa for the cast palms before failure, in both cases observed at the interface), demonstrating the stronger interfaces of printed palms. However, it was noted that the bending angle was wider for the cast palms (up to ~ 25 versus $\sim 22.5^\circ$). This could be due to slight differences in wall thicknesses or corner geometries between the printed and cast palms.

Finally, the robustness of the palms was assessed by conducting cyclic tests: the palms were inflated at three different pressures (10, 15, and 20 kPa) for 3 s, then deflated for 3 s, and a pressure sensor connected in series with the palm was used to record the palm pressure. At any cycle, if the pressure sensor reading dropped below the actuation pressure, the palm was checked for leakages and failures. Results averaged from three palm prototypes are shown in Figure 7f, with the raw data reported in Section S11. The printed palms could withstand a significantly higher number of cycles compared to the cast palm across by a factor of 13, 9, and 5 at 10, 15, and 20 kPa, respectively. It can be concluded that the life expectancy of functional components manufactured by FL-3DP was significantly improved compared to cast components. On a side note, it should be highlighted that the robustness of the palm could easily be tuned by selecting different materials compared to those presented in this study.

3. CONCLUSIONS

In this work, a FL-3DP approach was developed and optimized for the manufacturing of RTV silicones into robust functional multimaterial components with complex 3D structures. With the help of an in-depth analysis of the rheological interactions between the inks and support and the impact of operational parameters on the filament shape, multiple materials could be combined into functional structures with high fidelity. The advantages of FL-3DP over traditional casting methods were then demonstrated through the fabrication of soft components suitable for soft robotics. First, sensorized sleeves were designed to customize FPA. The combination of multiple materials, functional strain sensors, and complex features such as pillars, enabled a high degree of customization and tunability of gripping performances (bending, normal force, wrapping force, adaptation to the type of payload). Second, 3D-printed

inflatable multimaterial palms could withstand higher pressures (by a factor of 1.6) and exhibited a significant increase in life expectancy (by a factor of up to 13) compared to cast palms, demonstrating the enhancement of material interfaces when using FL-3DP. With the emergence of novel materials not always processable through traditional additive manufacturing technologies, such as hybrids displaying a large range of elasticities,⁵ FL-3DP stands to broaden the impact of additive manufacturing, enabling the processing of a much wider materials library, and opening design possibilities in various applications such as soft robotics.

4. MATERIALS AND METHODS

4.1. Materials. Ecoflex 00-30, SORTA-Clear 12, Smooth-Sil 960, THI-VEX, SLO-JO, silicone thinner, and pigments (SIL-PIG) were purchased from Smooth-On (PA). All materials were thoroughly mixed before use. Laponite XLG clay particles were purchased from BYK additives (Germany). The chemicals were used as received and were not further purified.

4.2. Ink Formulations. Ecoflex 00-30 was prepared by first manually premixing part B in a syringe (30 cm 3) with the retardant SLO-JO (1:50 weight ratio to part B), increasing the inkpot life to ~ 3 h. Part A was added to the mixture (1:1 weight ratio to part B) and premixed before adding THI-VEX to create thixotropicity (1:50 weight ratio to part A) and the colorant. After thorough manual mixing, the syringe content was further homogenized for 2 min at 2000 rpm followed by 5 min defoaming at 2200 rpm using an ARE-310 planetary mixer (Thinky mixer; Tokyo, Japan). Similarly, SORTA-Clear 12 was prepared by manually mixing part B in a syringe (30 cm 3) with the retardant SLO-JO (1:25 weight ratio to part B). Part A was added to the mixture and premixed (1:1 weight ratio to part B) before adding THI-VEX (1:100 weight ratio to part A) and the colorant. After thorough mixing, the syringe content was further homogenized for 2 min at 2000 rpm followed by 5 min defoaming at 2200 rpm using an ARE-310 planetary mixer (Thinky mixer; Tokyo, Japan). Finally, Smooth-Sil 960 was prepared by mixing part B, silicone thinner (1:1.5 weight ratio to part B), SLO-JO (1:3.75 weight ratio to part B), and THI-VEX (1:30 weight ratio to part B). After thorough mixing, part A was added (10:1 weight ratio to part B), manually mixed, and further homogenized with the planetary mixer (2 min at 2000 rpm followed by 5 min defoaming at 2200 rpm).

4.3. Bath Formulation. A nanoclay-based Laponite support bath was prepared as follows: Laponite powder was weighed and delicately dispersed in deionized water (18.2 M Ω ·cm), followed by 1 h of vigorous stirring at 60 $^\circ$ C to help the dissolution of aggregates. The resulting bath was defoamed at 2200 rpm for 2 min using an ARE-310 planetary mixer and poured in a container. The bath was left at rest for 4 h prior to printing.

4.4. Printing. The printing of functional sleeves was conducted on a commercially available 3D printer (System 30M, Hyrel Inc.), which provided a multipurpose three-axis motion system. The fluid extrusion was carried out using a pneumatic fluid dispensing system (Ultimus V, Nordson EFD; Westlake, OH), with disposable 30 mL Luer-tipped syringes attached to the 3D printer with a custom-made adapter. All inks were extruded with a 20-gauge stainless steel needle (McMaster, inner diameter of 0.66 mm, outer diameter of 0.91 mm, length of 38.1 mm), except the textured pillars that were extruded with a 45 $^\circ$ bent needle (McMaster, 45 $^\circ$ angle, 0.97 mm inner diameter, 25.4 mm length). G-code to fabricate each sample part was automatically generated from CAD designs using open-source software Slic3r. The layering in the XY-direction was calculated by Slic3r with a filament diameter set to 0.6 mm. The layering in the Z-direction was manually set according to the ink properties. For bases requiring to fill an entire area (two layers minimum), three perimeter lines were first printed followed by a perpendicular infill with an overlapping of 150% to ensure fusion between the perimeter and infill.

4.5. Rheological Characterization. The rheological properties of the inks were characterized using a controlled stress rheometer

(Discovery HR-2 Hybrid rheometer, TA Instruments). A 40 mm conical plate geometry (2°) was used with a gap set to 100 μm . The viscoelastic region of the support was first checked via a frequency sweep conducted from 0.01 to 300 $\text{rad}\cdot\text{s}^{-1}$. The flow ramp measurements for studying shear-thinning behavior were carried out at a frequency of 1 Hz within the stress range of 0.01–2000 Pa at 25 $^\circ\text{C}$ under a closed-loop temperature control for 60 s. The oscillatory stress sweeps of samples in the linear viscoelastic region were performed in the 0.1–2000 $\text{rad}\cdot\text{s}^{-1}$ range with a frequency of 1 Hz to measure G' and G'' .

4.6. Microscopy. The line diameters of extruded inks and the images of the printed components were obtained using a digital 3D microscope KH-8700 (Hirox) equipped with an MXG-10C lens and an OL-35 objective lens.

4.7. Characterization of the Sleeves. The gripper was mounted on a custom-made platform and connected to a pressure dispenser (Ultimus V, Nordson EFD). The change of curvature was determined by recording the gripper under five actuation cycles, each cycle consisting of a steady pulse of pressure held for 2 s. Curvatures were measured and averaged. The change in voltage was simultaneously recorded. The blocking force and unwrapping force tests were conducted on a custom-made platform, with a load cell of 50 N (Sparkfun TAL220B). The force was measured at a frequency of 5 Hz. Experiments were repeated three times and averaged.

4.8. Palm Casting. Fabrication of the cast palm can be seen in Section S9 and consists of the following steps: a three-piece FDM printed mold was assembled and SC12 was injected into the mold assembly to cast the bellows. Once cured, the central piece of the mold assembly was replaced with another piece. SS960 was then injected into this new mold assembly to form the top and sidewalls of the palm. Upon curing, the palm bellows and walls were carefully demolded. In another FDM printed mold, SS960 was poured to form the bottom surface for the palm, on which the palm bellows and walls were carefully positioned. A silicone tube was inserted through a hole in the bottom surface and the hole was sealed using SS960.

4.9. Palm Characterization. Tensile tests were conducted on multilayered tensile specimens of dimensions adapted from ASTM D 412C (10 mm \times 15 mm \times 4 mm each side). Monomaterial specimens were studied to compare the impact of additives used in FL-3DP and the results are discussed in Section S12. To compare the performance of the cast and printed palms, finger adapters (ASA) were printed using a Fortus 450mc and glued to the palm sides using Loctite 731 and POP Primer. The palm was actuated using a silicone tube connected to the bottom of the palm using positive pressure held for 3 s and the palm bending angle was calculated using ImageJ software.

4.10. Simulations. Simulations for the palm and fabric actuator/sleeve were conducted using Abaqus (Dassault Systemes). The fabric actuator was modeled as an enclosed 3D deformable solid and the sleeve modeled as a 3D deformable shell (skin of the fabric actuator with a shell thickness of 0.1 mm). The increase of pressure was modeled using a fluid cavity inside the fabric actuator. The hollow trefoil-shaped chamber was modeled as a 3D deformable shell with a uniform shell thickness of 0.5 mm. To mimic the rigid finger adapters, inextensible skins were used at the three sidewalls of the hollow chamber. A pressure load was applied to the interior walls of the chamber, while an ENCASTRE boundary condition was applied to the center of the chamber base. The materials used and their constitutive material relations are reported in Section S12, and quadrilateral mesh elements (S4R) were used for the entire model. To assess the validity of our models, comparisons between the experimental and simulated curvatures of the fabric actuator on one hand, and the experimental and simulated bending angles of the multilayered palm, on the other hand, are provided in Section S12.

■ ASSOCIATED CONTENT

SI Supporting Information

The Supporting Information is available free of charge at <https://pubs.acs.org/doi/10.1021/acsami.1c20209>.

Viscosity as a function of the shear rate for Laponite-based support baths (Section S1); fitting the flow curves of the support bath with the Herschel–Bulkley model (Section S2); rheological properties of the support bath from oscillatory experiments (Section S3); self-healing of the support bath (Section S4); material properties of silicone rubbers (Section S5); fitting the flow curves of the silicone-based inks with the Herschel–Bulkley model (Section S6); rheological properties of the inks from oscillatory experiments (Section S7); filament extrusion in a 4.5 wt % bath (Section S8); unwrap force of functional sleeves (Section S9); palm casting (Section S10); cyclic tests for the palm inflation (Section S11); and mechanical properties of silicone rubbers and Abaqus simulations (Section S12) (PDF)

FL-3DP of sensorized composite sleeves (Movie S1) (MP4)

FL-3DP of textured composite sleeves (Movie S2) (MP4)

FL-3DP of multimaterial pneumatic palms (Movie S3) (MP4)

Sleeve unwrapping on the edged ring (Movie S4) (MP4)

■ AUTHOR INFORMATION

Corresponding Author

Pablo Valdivia y Alvarado – Digital Manufacturing and Design (DManD) Centre, Singapore University of Technology and Design, 487372, Singapore; Engineering and Product Development Pillar, Singapore University of Technology and Design, 487372, Singapore; orcid.org/0000-0003-0289-0628; Email: pablov@sutd.edu.sg

Authors

Théo Calais – Digital Manufacturing and Design (DManD) Centre, Singapore University of Technology and Design, 487372, Singapore; orcid.org/0000-0002-7485-9796

Naresh D. Sanandiyaa – Digital Manufacturing and Design (DManD) Centre, Singapore University of Technology and Design, 487372, Singapore; Present Address: School of Engineering, Newcastle University, Newcastle upon Tyne NE1 7RU, United Kingdom; orcid.org/0000-0001-6116-5237

Snehal Jain – Digital Manufacturing and Design (DManD) Centre, Singapore University of Technology and Design, 487372, Singapore; orcid.org/0000-0003-3437-0707

Elgar V. Kanhere – Digital Manufacturing and Design (DManD) Centre, Singapore University of Technology and Design, 487372, Singapore; orcid.org/0000-0002-9416-0931

Siddharth Kumar – Engineering and Product Development Pillar, Singapore University of Technology and Design, 487372, Singapore; orcid.org/0000-0003-3606-5060

Raye Chen-Hua Yeow – Department of Biomedical Engineering, National University of Singapore, 117583, Singapore

Complete contact information is available at: <https://pubs.acs.org/doi/10.1021/acsami.1c20209>

Notes

The authors declare no competing financial interest.

The raw data required to reproduce these findings are available from the corresponding author on reasonable request.

ACKNOWLEDGMENTS

This research project was supported by A*STAR under its Science and Engineering Research Council (SERC) Awards 1822500053 and W2025d0243. The authors would like to thank Jin-Huat Low and Phone-May Khin from the Department of Biomedical Engineering, College of Design and Engineering (NUS) for facilitating the use of their fabric-based pneumatic actuators for this study.

REFERENCES

- (1) McCormack, A.; Highley, C. B.; Leslie, N. R.; Melchels, F. P. W. 3D Printing in Suspension Baths: Keeping the Promises of Bioprinting Afloat. *Trends Biotechnol.* **2020**, *38*, 584–593.
- (2) Chen, S.; Tan, W. S.; Bin Juhari, M. A.; Shi, Q.; Cheng, X. S.; Chan, W. L.; Song, J. Freeform 3D Printing of Soft Matters: Recent Advances in Technology for Biomedical Engineering. *Biomed. Eng. Lett.* **2020**, *10*, 453–479.
- (3) Calais, T.; Alvarado, P. V. y. Advanced Functional Materials for Soft Robotics: Tuning Physicochemical Properties beyond Rigidity Control. *Multifunct. Mater.* **2019**, *2*, No. 042001.
- (4) Majidi, C. Soft-Matter Engineering for Soft Robotics. *Adv. Mater. Technol.* **2019**, *4*, No. 1800477.
- (5) Joseph, V. S.; Calais, T.; Stalin, T.; Jain, S.; Thanigaivel, N. K.; Sanandiyaa, N. D.; Valdivia y Alvarado, P. Silicone/Epoxy Hybrid Resins with Tunable Mechanical and Interfacial Properties for Additive Manufacture of Soft Robots. *Appl. Mater. Today* **2021**, *22*, No. 100979.
- (6) Schmitt, F.; Piccin, O.; Barbé, L.; Bayle, B. Soft Robots Manufacturing: A Review. *Front. Robot. AI* **2018**, *5*, No. 84.
- (7) Subramaniam, V.; Jain, S.; Agarwal, J.; Valdivia y Alvarado, P. Design and Characterization of a Hybrid Soft Gripper with Active Palm Pose Control. *Int. J. Rob. Res.* **2020**, 1668.
- (8) Shintake, J.; Caccuciolo, V.; Floreano, D.; Shea, H. Soft Robotic Grippers. *Adv. Mater.* **2018**, *30*, No. 1707035.
- (9) Zhang, Y.-F.; Ng, C. J.-X.; Chen, Z.; Zhang, W.; Panjwani, S.; Kowsari, K.; Yang, H. Y.; Ge, Q. Miniature Pneumatic Actuators for Soft Robots by High-Resolution Multimaterial 3D Printing. *Adv. Mater. Technol.* **2019**, *4*, No. 1900427.
- (10) Li, S.; Vogt, D. M.; Rus, D.; Wood, R. J. Fluid-Driven Origami-Inspired Artificial Muscles. *Proc Natl Acad Sci U.S.A.* **2017**, *114*, 13132–13137.
- (11) Stano, G.; Percoco, G. Additive Manufacturing Aimed to Soft Robots Fabrication: A Review. *Extreme Mech. Lett.* **2021**, *42*, No. 101079.
- (12) Walker, S.; Lingle, E.; Troxler, N.; Wallin, T.; Healy, K.; Mengüç, Y.; Davidson, J. R. Predicting Interfacial Layer Adhesion Strength in 3D Printable Silicone. *Addit. Manuf.* **2021**, *47*, No. 102320.
- (13) Wallin, T. J.; Simonsen, L.-E.; Pan, W.; Wang, K.; Giannelis, E.; Shepherd, R. F.; Mengüç, Y. 3D Printable Tough Silicone Double Networks. *Nat. Commun.* **2020**, *11*, No. 4000.
- (14) Roach, D. J.; Hamel, C. M.; Dunn, C. K.; Johnson, M. V.; Kuang, X.; Qi, H. J. The M4 3D Printer: A Multi-Material Multi-Method Additive Manufacturing Platform for Future 3D Printed Structures. *Addit. Manuf.* **2019**, *29*, No. 100819.
- (15) Stalin, T.; Thanigaivel, N. K.; Joseph, V. S.; Alvarado, P. V. In *Automated Fiber Embedding for Tailoring Mechanical and Functional Properties of Soft Robot Components*, 2019 2nd IEEE International Conference on Soft Robotics (RoboSoft), 2019; pp 762–767.
- (16) Han, D.; Lee, H. Recent Advances in Multi-Material Additive Manufacturing: Methods and Applications. *Curr. Opin. Chem. Eng.* **2020**, *28*, 158–166.
- (17) Peng, X.; Kuang, X.; Roach, D. J.; Wang, Y.; Hamel, C. M.; Lu, C.; Qi, H. J. Integrating Digital Light Processing with Direct Ink Writing for Hybrid 3D Printing of Functional Structures and Devices. *Addit. Manuf.* **2021**, *40*, No. 101911.
- (18) Cheng, W.; Zhang, J.; Liu, J.; Yu, Z. Granular Hydrogels for 3D Bioprinting Applications. *View* **2020**, *1*, No. 20200060.
- (19) Bhattacharjee, T.; Zehnder, S. M.; Rowe, K. G.; Jain, S.; Nixon, R. M.; Sawyer, W. G.; Angelini, T. E. Writing in the Granular Gel Medium. *Sci. Adv.* **2015**, *1*, No. e1500655.
- (20) Hinton, T. J.; Hudson, A.; Pusch, K.; Lee, A.; Feinberg, A. W. 3D Printing PDMS Elastomer in a Hydrophilic Support Bath via Freeform Reversible Embedding. *ACS Biomater. Sci. Eng.* **2016**, *2*, 1781–1786.
- (21) Jin, Y.; Compaan, A.; Bhattacharjee, T.; Huang, Y. Granular Gel Support-Enabled Extrusion of Three-Dimensional Alginate and Cellular Structures. *Biofabrication* **2016**, *8*, No. 025016.
- (22) Abdollahi, S.; Markvicka, E. J.; Majidi, C.; Feinberg, A. W. 3D Printing Silicone Elastomer for Patient-Specific Wearable Pulse Oximeter. *Adv. Healthcare Mater.* **2020**, *9*, No. 1901735.
- (23) Friedrich, L.; Begley, M. Changes in Filament Microstructures During Direct Ink Writing with a Yield Stress Fluid Support. *ACS Appl. Polym. Mater.* **2020**, *2*, 2528–2540.
- (24) Hinton, T. J.; Jallerat, Q.; Palchesko, R. N.; Park, J. H.; Grodzicki, M. S.; Shue, H.-J.; Ramadan, M. H.; Hudson, A. R.; Feinberg, A. W. Three-Dimensional Printing of Complex Biological Structures by Freeform Reversible Embedding of Suspended Hydrogels. *Sci. Adv.* **2015**, *1*, No. e1500758.
- (25) Lee, A.; Hudson, A. R.; Shiwardski, D. J.; Tashman, J. W.; Hinton, T. J.; Yerneni, S.; Bliley, J. M.; Campbell, P. G.; Feinberg, A. W. 3D Bioprinting of Collagen to Rebuild Components of the Human Heart. *Science* **2019**, *365*, 482–487.
- (26) Mirdamadi, E.; Tashman, J. W.; Shiwardski, D. J.; Palchesko, R. N.; Feinberg, A. W. FRESH 3D Bioprinting a Full-Size Model of the Human Heart. *ACS Biomater. Sci. Eng.* **2020**, *6*, 6453–6459.
- (27) Ding, H.; Chang, R. C. Printability Study of Bioprinted Tubular Structures Using Liquid Hydrogel Precursors in a Support Bath. *Appl. Sci.* **2018**, *8*, No. 403.
- (28) Tan, W. S.; Juhari, M. A. B.; Shi, Q.; Chen, S.; Campolo, D.; Song, J. Development of a New Addit. Manuf. Platform for Direct Freeform 3D Printing of Intrinsically Curved Flexible Membranes. *Addit. Manuf.* **2020**, *36*, No. 101563.
- (29) Highley, C. B.; Rodell, C. B.; Burdick, J. A. Direct 3D Printing of Shear-Thinning Hydrogels into Self-Healing Hydrogels. *Adv. Mater.* **2015**, *27*, 5075–5079.
- (30) Chen, S.; Jang, T.-S.; Pan, H. M.; Jung, H.-D.; Sia, M. W.; Xie, S.; Hang, Y.; Chong, S. K. M.; Wang, D.; Song, J. 3D Freeform Printing of Nanocomposite Hydrogels through in Situ Precipitation in Reactive Viscous Fluid. *Int. J. Bioprint.* **2020**, *6*, No. 258.
- (31) Shin, S.; Hyun, J. Matrix-Assisted Three-Dimensional Printing of Cellulose Nanofibers for Paper Microfluidics. *ACS Appl. Mater. Interfaces* **2017**, *9*, 26438–26446.
- (32) Uchida, T.; Onoe, H. 4D Printing of Multi-Hydrogels Using Direct Ink Writing in a Supporting Viscous Liquid. *Micromachines* **2019**, *10*, No. 433.
- (33) Jin, Y.; Chai, W.; Huang, Y. Printability Study of Hydrogel Solution Extrusion in Nanoclay Yield-Stress Bath during Printing-Then-Gelation Biofabrication. *Mater. Sci. Eng., C* **2017**, *80*, 313–325.
- (34) Jin, Y.; Compaan, A.; Chai, W.; Huang, Y. Functional Nanoclay Suspension for Printing-Then-Solidification of Liquid Materials. *ACS Appl. Mater. Interfaces* **2017**, *9*, 20057–20066.
- (35) Jin, Y.; Chai, W.; Huang, Y. Fabrication of Stand-Alone Cell-Laden Collagen Vascular Network Scaffolds Using Fugitive Pattern-Based Printing-Then-Casting Approach. *ACS Appl. Mater. Interfaces* **2018**, *10*, 28361–28371.
- (36) Rodriguez, M. J.; Dixon, T. A.; Cohen, E.; Huang, W.; Omenetto, F. G.; Kaplan, D. L. 3D Freeform Printing of Silk Fibroin. *Acta Biomater.* **2018**, *71*, 379–387.
- (37) Mahmoudi, M.; Burlison, S. R.; Moreno, S.; Minary-Jolandan, M. Additive-Free and Support-Free 3D Printing of Thermosetting Polymers with Isotropic Mechanical Properties. *ACS Appl. Mater. Interfaces* **2021**, *13*, 5529–5538.

- (38) Jin, Y.; Song, K.; Gellermann, N.; Huang, Y. Printing of Hydrophobic Materials in Fumed Silica Nanoparticle Suspension. *ACS Appl. Mater. Interfaces* **2019**, *11*, 29207–29217.
- (39) Compaan, A. M.; Song, K.; Huang, Y. Gellan Fluid Gel as a Versatile Support Bath Material for Fluid Extrusion Bioprinting. *ACS Appl. Mater. Interfaces* **2019**, *11*, 5714–5726.
- (40) Wang, Z.; Floryczyk, S. J. Freeze-FRESH: A 3D Printing Technique to Produce Biomaterial Scaffolds with Hierarchical Porosity. *Materials* **2020**, *13*, No. 354.
- (41) Song, K. H.; Highley, C. B.; Rouff, A.; Burdick, J. A. Complex 3D-Printed Microchannels within Cell-Degradable Hydrogels. *Adv. Funct. Mater.* **2018**, *28*, No. 1801331.
- (42) Shi, L.; Carstensen, H.; Hölzl, K.; Lunzer, M.; Li, H.; Hilborn, J.; Ovsianikov, A.; Ossipov, D. A. Dynamic Coordination Chemistry Enables Free Directional Printing of Biopolymer Hydrogel. *Chem. Mater.* **2017**, *29*, 5816–5823.
- (43) O'Bryan, C. S.; Bhattacharjee, T.; Hart, S.; Kabb, C. P.; Schulze, K. D.; Chilakala, I.; Sumerlin, B. S.; Sawyer, W. G.; Angelini, T. E. Self-Assembled Micro-Organogels for 3D Printing Silicone Structures. *Sci. Adv.* **2017**, *3*, No. e1602800.
- (44) Hajash, K.; Sparrman, B.; Guberan, C.; Laucks, J.; Tibbits, S. Large-Scale Rapid Liquid Printing. *3D Print. Addit. Manuf.* **2017**, *4*, 123–132.
- (45) O'Bryan, C. S.; Bhattacharjee, T.; Niemi, S. R.; Balachandar, S.; Baldwin, N.; Ellison, S. T.; Taylor, C. R.; Sawyer, W. G.; Angelini, T. E. Three-Dimensional Printing with Sacrificial Materials for Soft Matter Manufacturing. *MRS Bull.* **2017**, *42*, 571–577.
- (46) Hughes, J.; Culha, U.; Giardina, F.; Guenther, F.; Rosendo, A.; Iida, F. Soft Manipulators and Grippers: A Review. *Front. Robot. AI* **2016**, *3*, No. 69.
- (47) Jain, S.; Stalin, T.; Subramaniam, V.; Agarwal, J.; Valdivia y Alvarado, P. In *A Soft Gripper with Retractable Nails for Advanced Grasping and Manipulation*, 2020 IEEE International Conference on Robotics and Automation (ICRA) 2020; pp 6928–6934.
- (48) Low, J. H.; Cheng, N.; Khin, P. M.; Thakor, N. V.; Kukreja, S. L.; Ren, H. L.; Yeow, C. H. In *A Bidirectional Soft Pneumatic Fabric-Based Actuator for Grasping Applications*, 2017 IEEE/RSJ International Conference on Intelligent Robots and Systems (IROS), 2017; pp 1180–1186.
- (49) Fei, Y.; Wang, J.; Pang, W. A Novel Fabric-Based Versatile and Stiffness-Tunable Soft Gripper Integrating Soft Pneumatic Fingers and Wrist. *Soft Rob.* **2019**, *6*, 1–20.
- (50) Thompson, D. W.; Butterworth, J. T. The Nature of Laponite and Its Aqueous Dispersions. *J. Colloid Interface Sci.* **1992**, *151*, 236–243.
- (51) Dinkgreve, M.; Paredes, J.; Denn, M. M.; Bonn, D. On Different Ways of Measuring “the” Yield Stress. *J. Non-Newtonian Fluid Mech.* **2016**, *238*, 233–241.
- (52) Ghica, M. V.; Hirjau, M.; Lupuleasa, D.; Dinu-Pirvu, C.-E. Flow and Thixotropic Parameters for Rheological Characterization of Hydrogels. *Molecules* **2016**, *21*, No. 786.
- (53) Grosskopf, A. K.; Truby, R. L.; Kim, H.; Perazzo, A.; Lewis, J. A.; Stone, H. A. Viscoplastic Matrix Materials for Embedded 3D Printing. *ACS Appl. Mater. Interfaces* **2018**, *10*, 23353–23361.
- (54) Jiang, T.; Munguia-Lopez, J. G.; Flores-Torres, S.; Kort-Mascort, J.; Kinsella, J. M. Extrusion Bioprinting of Soft Materials: An Emerging Technique for Biological Model Fabrication. *Appl. Phys. Rev.* **2019**, *6*, No. 011310.
- (55) Chilton, R. A.; Stainsby, R. Pressure Loss Equations for Laminar and Turbulent Non-Newtonian Pipe Flow. *J. Hydraul. Eng.* **1998**, *124*, 522–529.
- (56) Jain, S.; Stalin, T.; Kanhere, E.; Valdivia y Alvarado, P. Flexible Fiber Interconnects for Soft Mechatronics. *IEEE Rob. Autom. Lett.* **2020**, *5*, 3907–3914.
- (57) Rosset, S.; Shea, H. R. Flexible and Stretchable Electrodes for Dielectric Elastomer Actuators. *Appl. Phys. A: Mater. Sci. Process.* **2013**, *110*, 281–307.

Recommended by ACS

3D Printing of Liquid Metal Embedded Elastomers for Soft Thermal and Electrical Materials

Phillip Won, Carmel Majidi, *et al.*

DECEMBER 02, 2022
ACS APPLIED MATERIALS & INTERFACES

READ 

A High-Fidelity Preparation Method for Liquid Crystal Elastomer Actuators

Yaoyao Jiang, Jianing Ding, *et al.*

MAY 28, 2022
LANGMUIR

READ 

RAFT-Mediated 3D Printing of “Living” Materials with Tailored Hierarchical Porosity

Mitra Asadi-Eydivand, Ali Bagheri, *et al.*

JUNE 28, 2022
ACS APPLIED POLYMER MATERIALS

READ 

Three-Dimensional Printable, Extremely Soft, Stretchable, and Reversible Elastomers from Molecular Architecture-Directed Assembly

Shifeng Nian, Li-Heng Cai, *et al.*

MARCH 31, 2021
CHEMISTRY OF MATERIALS

READ 

Get More Suggestions >